Article PDF Available

# Exploring the Influence of Temperature and Time on the Formation and Properties of 3D Flower-Like MoS2 Nanostructures Synthesized via Hydrothermal Method

IOP Publishing ECS Journal of Solid State Science and Technology

September 2023 · 12(9)

DOI:10.1149/2162-8777/acf8f1

**Authors:**

**Ritu Kumari**

**Rakesh Kumar**
Central University of Haryanaa

Citations (3) References (68) Figures (9)

Abstract and Figures

A simple hydrothermal method was employed to synthesize 3D flower-like MoS2 nanostructures. The influence of different synthesis temperatures on the structural, electronic, optical and morphological properties of the MoS2 nanostructures was thoroughly investigated, and the optimal temperature was identified as 220℃. Additionally, we conducted further optimization to determine the most suitable reaction time, which was found to be 24 hours. The characterization of the synthesized MoS2 nanostructures, employing various techniques such as X-ray diffraction, Raman spectroscopy, Mott-Schottky analysis, UV-Vis-NIR spectroscopy, and field-emission scanning electron microscopy, unveiled well-defined crystallinity, reduced thickness, and uniform morphology, under optimized conditions. Notably, as the temperature increased from 180 to 220℃, the band gap of MoS2 nanostructures exhibited a notable increase from 1.72 to 2.35 eV. The Mott-Schottky analysis further confirmed our findings, revealing lower values of flat band potential and carrier concentration for the optimized temperature (220℃), indicative of higher crystallinity with fewer defects. These comprehensive findings not only underscore the significant impact of temperature and time on the properties of MoS2 nanostructures but also hold promising implications for diverse applications, including sensing, energy storage, as well as photocatalysis for hydrogen evolution reactions and organic pollutant degradation.

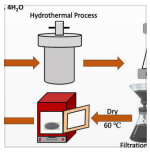


Schematic representation …

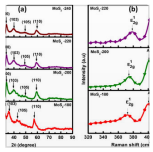

(a) X-ray diffraction…

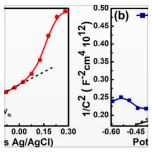


Mott-Schottky plots of MoS2…

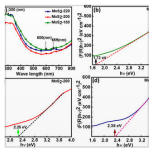

(a) Absorbance spectra of MoS…

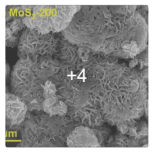


FESEM images of MoS2…

Figures - uploaded by Rakesh Kumar Author content

*ECS Journal of Solid State Science and Technology*, 2023 **12** 097004
2162-8777/2023/12(9)/097004/10/$40.00 © 2023 The Electrochemical Society ("ECS"). Published on behalf of ECS by IOP Publishing Limited

# Exploring the Influence of Temperature and Time on the Formation and Properties of 3D Flower-Like $MoS_2$ Nanostructures Synthesized via Hydrothermal Method

**Ritu Kumari and Rakesh Kumar**[z]

*Department of Physics and Astrophysics, Central University of Haryana, Mahendergarh –123031, India*

In this study, a simple hydrothermal method was employed to synthesize 3D flower-like $MoS_2$ nanostructures. The influence of different synthesis temperatures on the structural, electronic, optical and morphological properties of the $MoS_2$ nanostructures was thoroughly investigated, and the optimal temperature was identified as 220 °C. Additionally, we conducted further optimization to determine the most suitable reaction time, which was found to be 24 h. The characterization of the synthesized $MoS_2$ nanostructures, employing various techniques such as X-ray diffraction, Raman spectroscopy, Mott-Schottky analysis, UV–vis-NIR spectroscopy and field emission scanning electron microscopy, unveiled well-defined crystallinity, reduced thickness and uniform morphology, under the optimized conditions. Notably, as the temperature increased from 180 °C to 220 °C, the band gap of $MoS_2$ nanostructures exhibited a notable increase from 1.72 to 2.35 eV. The Mott-Schottky analysis further confirmed our findings, revealing lower values of flat band potential and carrier concentration for the optimized temperature (220 °C), indicative of higher crystallinity with fewer defects. These comprehensive findings not only underscore the significant impact of temperature and time on the properties of $MoS_2$ nanostructures but also hold promising implications for diverse applications, including sensing, energy storage, as well as photocatalysis for hydrogen evolution reactions and organic pollutant degradation.
 [DOI: 10.1149/2162-8777/acf8f1]

Manuscript submitted May 15, 2023; revised manuscript received August 9, 2023. Published September 20, 2023.

Two-dimensional (2D) transition metal dichalcogenides (TMDs) materials have gained immense research interests owing to their promising electrical, mechanical, optical and chemical properties.[1–6] These materials, including $MoS_2$, $WS_2$, $MoSe_2$, $VS_2$, $WSe_2$ and many more, have shown great potentials for use in various applications, such as electronic devices, gas sensing devices, energy storage devices, hydrogen evolution reactions, solar cells, lubricants, etc.[2,7–14] $MoS_2$, as one of the representative members of TMDs, is a well-known two-dimensional (2D) material. Like graphene, $MoS_2$ consists of a layered structure in which a layer of molybdenum atoms is sandwiched between two layers of hexagonally packed sulphur atoms with strong covalent bonds (S-Mo-S). The layers of $MoS_2$ are attached together by weak van der Waals forces of attraction.[15–19] Depending on the stacking sequence and Mo-S coordination, $MoS_2$ exists in different polytypes, such as 1H, 2H, 1 T, and 3 R.[18,20] Among these polytypes, 1H and 2H phases are more stable with trigonal prismatic coordination than other metastable phases of 3 R and 1 T. The 3 R and 1 T polytypes of $MoS_2$ can be easily transferred into the 2H phase via heating. The 2H and 3 R phases of $MoS_2$possess semiconducting properties and diamagnetic in nature. Moreover, the 1 T phase of $MoS_2$ shows metallic behaviour with paramagnetic nature. Previous studies have demonstrated that the 1 T phase has more reactive sites than other phases, which provides better facile route for surface functionalization.[21,22] Interestingly, owing to their superior semiconducting nature, $MoS_2$ has become an auspicious material for various application areas, such as optoelectronics, high speed electronics, energy storage, energy conversion and gas sensing as well as in bio sensing.

It has been shown that the synthesis method can play a crucial role not only in synthesizing the nanostructures with desired morphology but also in controlling their physiochemical properties.[23–27] Various physical as well as chemical methods can be used to synthesized $MoS_2$ nanostructures.[28] Depending on the synthesis method, $MoS_2$ nanostructures can be formed with different morphologies such as 2D sheets, plates, tubes, ribbons, 3D flower, sphere and so on.[29–31] Recently, the 3D flower-like morphology of $MoS_2$ nanostructures has gained enormous interest due to its various practical applications.[21,32,33] Several physical methods, including sputtering, laser ablation and pulse laser deposition have been used for the synthesis of $MoS_2$nanostructures.[15,30,34–36] Although most of physical method are very fast, and they involve a lot of complica procedures and costly instrumentation.[28] Moreover, the aggregat tendency of nanostructures synthesized by physical approaches also very high.[20] Chemical methods, such as chemical vap deposition, sol-gel, solvothermal and hydrothermal method, also be used to synthesize $MoS_2$ nanostructures.[37–40] Among chemical methods, the hydrothermal method is the simplest, m economical and versatile method.[16,30]

Hydrothermal synthesis is a highly promising method for large-scale production of $MoS_2$ and can be effectively combir with other processes. Remarkably, the unique combination temperature and pressure in hydrothermal solutions offers affordable and efficient approach for synthesizing different phases $MoS_2$.[41] For instance, Zhang et al. reported the hydrother synthesis of 3D flower-like hemispheres consisting of Mo nanosheets using hexadecyltrimethyl ammonium bromide (CTA as a surfactant, along with ammonia solution to control the solutio pH for various reaction times. However, the shorter duration of 1 resulted in the presence of impurities due to the surfactant CT content.[42] Another study by Zhang et al. demonstrated the synthe of nano/micro-spheres of $MoS_2$ at different temperatures us sodium molybdate dihydrate and thiourea as precursors. While samples synthesized at different temperatures displayed non-unifo morphologies with distinct nanorods and microsphere-like str tures, the addition of polyethylene glycol as a surfactant led t more uniform morphology.[31]

Furthermore, Vidhya et al. and Kumar et al. also conduc hydrothermal synthesis to produce $MoS_2$ nanoflakes and na flowers, respectively, at varying temperatures. Interestingly, reaction temperature did not significantly affect the number $MoS_2$ layers.[24,33] In a different study, Yang et al. successfu synthesized $MoS_2$ nanoflowers under diverse hydrothermal con tions, by adjusting the precursors of Mo, molar ratio of Mo reaction time, reaction temperature, and pH of the solution. T results indicated that $MoS_2$ nanoflowers exhibited a homogene dispersion when prepared with specific conditions, includ $H_{24}Mo_7N_6O_{24}$ and thiourea precursors, a 1:4 ratio of Mo/S hydrothermal temperature of 220 °C, an 1 .. hydrothermal ti and a pH value of 5.[29] Lin et al. also explored the possibility surfactant-assisted hydrothermal preparation to assemble Mo nanospheres consisting of a few layers of nanosheets.[39] Moreov Zhang et al. investigated the influence of the reaction time on formation of $MoS_2$ microspheres using hexaammoni

[z]E-mail: rks@cuh.ac.in

heptamolybdate tetrahydrate ($(NH_4)_6Mo_7O24$) and thiourea as precursors.[40] Similarly, Thang et al. synthesized $MoS_2$ nanoflowers with varying reaction times.[43] The effect of reaction time on $MoS_2$ layers was unclear in these studies, leaving a gap in our understanding of how the synthesized nanostructures grow and develop with time. Solving this puzzle is essential to fully harness the exciting properties of $MoS_2$ for various applications.

In this study, our primary focus was on hydrothermal synthesis, aiming to create 3D flower-like $MoS_2$ nanostructures. We conducted experiments varying the synthesis temperature between 180 °C and 240 °C to determine the optimal temperature for the best results. Subsequently, we explored the impact of reaction time, ranging from 3 to 48 h, to find the ideal duration for achieving excellent growth and crystallinity of the nanostructures. The outcomes unveiled that a temperature of 220 °C offered the most conducive conditions, resulting in well-defined crystallinity and a unique morphology of $MoS_2$ nanostructures. Moreover, a thorough analysis of various parameters, such as morphological details, layer thickness, uniformity and crystallinity, strongly suggested that a reaction time of 24 h, paired with a temperature of 220 °C, represented the most optimized conditions for the successful synthesis.

## Materials and Method

The chemicals used in this study, including Ammonium molybdatetrahydrate ($(NH_4)_6Mo_7O_{24}.4H_2O$, 99.9%), thiourea ($CH_4N_2S$ 99.9%), DI water and ethanol were purchased from Sigma Aldrich.

***Synthesis of $MoS_2$.***—$MoS_2$ was synthesized by using ammonium molybdate tetrahydrate [$(NH_4)_6Mo_7O_{24}4H_2O$] and thiourea [$CH_4N_2S$] as precursors for molybdenum and sulphur, respectively, without any further purification. The synthesis process (depicted in Fig. 1) began with the mixing of 1.072 g of ammonium molybdate tetrahydrate and 0.93 g of thiourea in 70 ml of deionized water under vigorous stirring at 800 rpm for an hour at a constant temperature of 30 °C. This resulted in a transparent and homogeneous solution, which was then transferred into a 100 ml Teflon-lined stainless-steel autoclave for heating treatment at different temperatures and times. After completion of the hydrothermal process, the autoclave was allowed to cool down to room temperature naturally. The resulting sample was then washed thoroughly with ethanol and deionized water by centrifugation at 4000 rpm. Finally, the resultant product was dried at 60 °C for 12 h in a hot air oven. The samples synthesized at temperatures of 180 to 240 °C were labelled as $MoS_2-180$, $MoS_2-200$, $MoS_2-220$ and $MoS_2-240$, respectively. Furthermore, to study the influence of reaction time on the $MoS_2$ nanostructures, different reaction times of 3, 6, 12, 24 and 48 h were used. The synthesized samples with different reaction times of 3, 6, 12, 24, and 48 h were labelled as MS-3, MS-6, MS-12, MS-24, MS-48, respectively.

***Material characterizations.***—For obtaining the crystallographic information of the synthesized samples, X-ray diffraction (XRD) patterns were recorded using a Rigaku instrument of smart lab with monochromatized Cu $K_\alpha$ radiation ($\lambda = 1.54$ Å) in the $2\theta$ range of 10°–70° and a scanning rate 5°/min. Raman spectra of the synthesized samples were recorded using a Raman spectrometer (Alpha 300/WTIC) with a laser power of 15 mW at an excitation wavelength of 532 nm. The morphological details of the samples were examined using NOVA Nanosem 450 and 7610 F Plus/JEOL field emission scanning electron microscope (FESEM). The optical properties of the samples were determined using a double beam UV–vis-NIR spectrophotometer (Cary5000, Agilent). Mott -Schottky analysis was carried out to confirm the semiconducting nature of the synthesized materials using Metrohm-Autolab.

## Results and Discussion

***Influence of temperature.***—The crystallographic structure of the hydrothermally synthesized $MoS_2$ nanostructures was thoroughly analyzed through X-ray diffraction patterns, as depicted in Fig. 2a. Remarkably, all diffraction peaks of the prepared samples perfectly matched the standard JCPDS data (37–1492) for the hexagonal $MoS_2$ crystal structure, indicating the presence of a pure phase of $MoS_2$ crystal without any additional peaks.[28,44,45] Notably, as the reaction temperature increased from 180 °C to 220 °C with a constant moderate reaction time of 24 h, the intensity and sharpness of all diffracted peaks also increased significantly. This phenomenon is attributed to the alignment of atom orientations in a specific direction as the reaction temperature rises, leading to improved crystalline quality and larger crystallite size.[21] However, the sharpness of the peak corresponding to the (002) plane decreased when

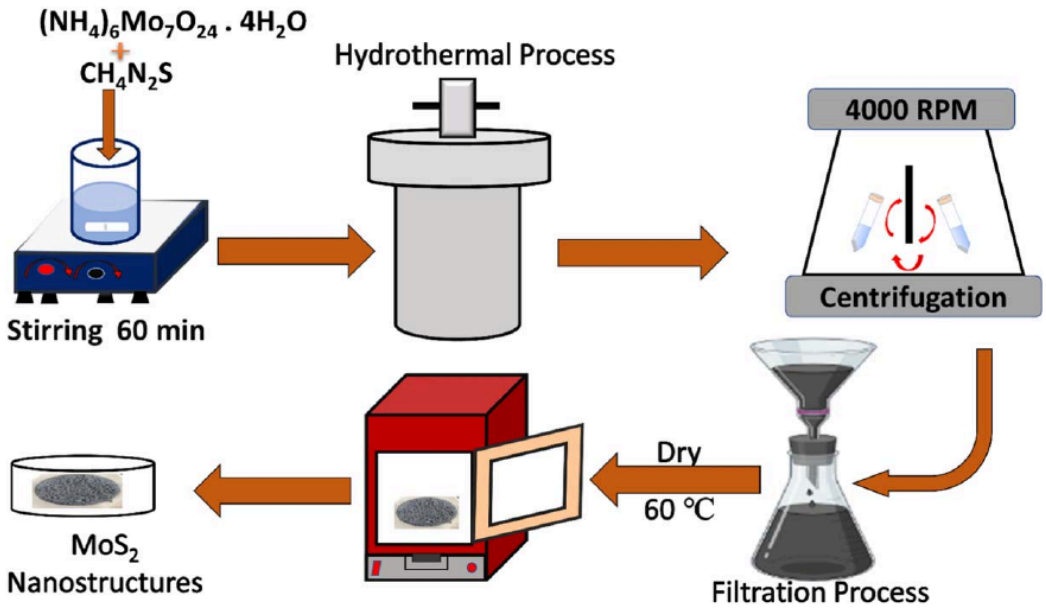


**Figure 1.** Schematic representation of hydrothermal synthesis of $MoS_2$.

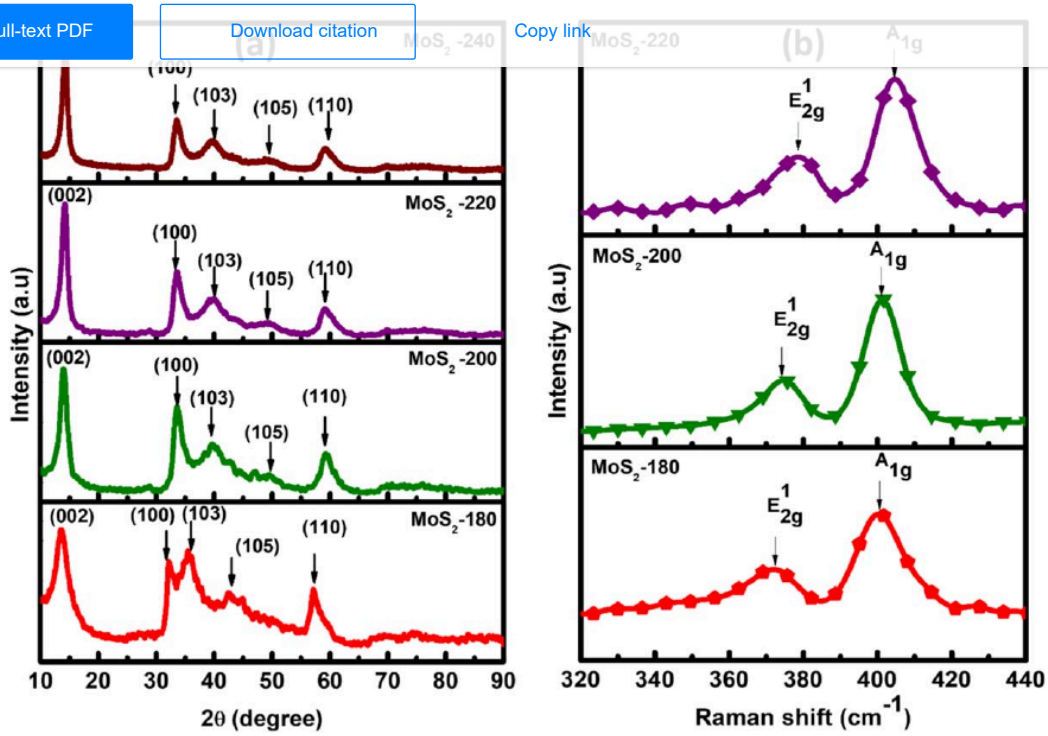


**Figure 2.** (a) X-ray diffraction patterns of as-synthesized samples at various temperatures ranging from 180 to 240 °C and (b) Raman spectra of samples synthesized at 180, 200, and 220 °C.

**Table I. Comparison of diffraction angle (2$\theta$), interlayer spacing (d), crystallite sizes (D), lattice constant (a, b c), microstrain ($\varepsilon$) and dislocation density ($\delta$) of as-synthesized MoS $_2$samples.**

| Sample | 2$\theta$ (hkl) | d (nm) | D (nm) | a = b (Å) | c (Å) | $\varepsilon$ | $\delta$(l $\times 10^{15}$/m$^{-2}$) |
|---|---|---|---|---|---|---|---|
| $MoS_2$ −180 | 13.84° (002) | 0.63 | 4.17 | 3.13 | 12.78 | 0.0087 | 57.3 |
| $MoS_2$ −200 | 13.80° (002) | 0.64 | 6.23 | 3.06 | 12.82 | 0.0058 | 25.7 |
| $MoS_2$ −220 | 14.26° (002) | 0.62 | 8.53 | 3.07 | 12.45 | 0.0042 | 13.7 |
| $MoS_2$ −240 | 14.34° (002) | 0.617 | 7.7 | 3.06 | 12.40 | 0.0047 | 16.9 |

the reaction temperature was further increased from 220 °C to 240 °C. This could be attributed to the bending of MoS $_2$ nanosheets under faster reaction conditions at higher temperatures, resulting in the introduction of defects and strain effects in the sample.[46,47]

It was observed that as the reaction temperature increased from 180 °C to 240 °C, the positions of the peaks shifted towards the right side, indicating a decrease in the interplanar spacing of the $MoS_2$ nanostructures synthesized at higher temperatures.[21] Notably, the ratio of peak intensity at 14.26° ($I_{002}$) to the peak intensity at 33.26° ($I_{100}$) increased with rising reaction temperature, suggesting that higher temperatures inhibited the lamellar growth and accumulation.[28] The strong peak at 14.26°, corresponding to the (002) plane, indicates the well-formed long-range stacking layers along the *c*-axis in the material.[21]

As the reaction temperature increased from 180 °C to 220 °C, the crystallite size of the materials gradually increased, while both the microstrain and dislocation density decreased. However, with a further temperature increased from 220 °C to 240 °C, the crystallite size decreased, and both microstrain and dislocation density increased. These changes, as shown in Table I, suggest that the sample synthesized at 220 °C exhibited better crystalline quality due to its larger crystallite size (8.53 nm) and lower microstrain (0.0042) and dislocation density (13.7 m$^{-2}$). Therefore, we considered 220 °C as the best-optimized temperature and utilized it for further studies.

Raman spectroscopy with a laser wavelength of 532 nm was used to further investigate the number of layers and crystallographic properties of as prepared $MoS_2$ nanostructures. In the Raman spectra of the $MoS_2$ samples (as shown in Fig. 2b, we can see two intense peaks at 378 and 404 cm$^{-1}$. These two peaks are the characteristics peaks of the hexagonal structure of the $MoS_2$ that arise due to in-plane ($E^1_{2g}$) and out-of-plane ($A_{1g}$) vibration modes of $MoS_2$, respectively.[48] The presence of these characteristic peaks in all three samples confirms the hexagonal phase of $MoS_2$ in all the prepared samples. It is clearly seen from the Raman spectra that the $E^1_{2g}$ and $A_{1g}$ peaks are blue-shifted as the reaction temperature



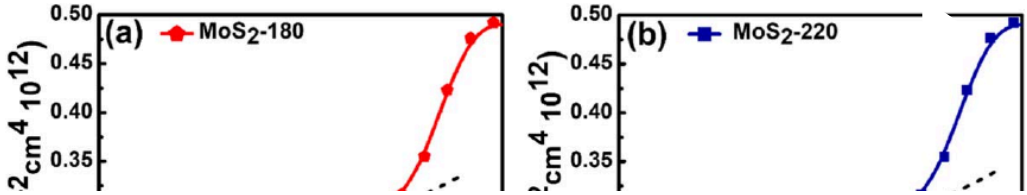

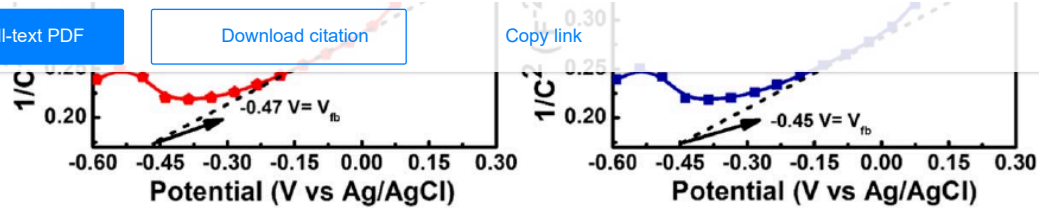


**Figure 3.** Mott-Schottky plots of $MoS_2$ samples prepared with 180 and 220 °C temperature.

increases from 180 to 220 °C. This is because of the suppression of interatomic vibration of van der Waals forces that leads to increased force constants with an increase in the number of layers.[49] It is well established that the difference in the Raman shift of $E^1_{2g}$ and $A_{1g}$ peaks can be used to determine the number of stacking layers of $MoS_2$ samples.[49] From Fig. 2b, we can see that the difference in the position of the $E^1_{2g}$ and $A_{1g}$ peaks decreases with an increase in temperature, indicating a decrease in the number of $MoS_2$ layers at higher temperature. Furthermore, $E^1_{2g}$ is related to the crystalline quality of the samples. Broadening and low intensity of this peak suggest the presence of some defects in the basal plane of $MoS_2$.[21] Here, we can see that with increasing hydrothermal temperature, the intensity and sharpness of this peak increases, revealing an improvement in crystalline quality and a reduction in structural defects. This observation is in good agreement with our XRD data. More specially, the lower intensity of the $E^1_{2g}$ peak than $A_{1g}$ peak suggests the edge-terminated $MoS_2$ of a few layers in all synthesized samples. Moreover, the intensity ratio of these $A_{1g}$ and $E^1_{2g}$ vibration modes also provides information about the intrinsic properties of materials.[50] The sample with a higher intensity ratio can be attributed to lower electron density. As the hydrothermal temperature increases from 180 to 220 °C, the intensity ratio also increases, suggesting a reduction in the electron density of the synthesized samples.[49] Additionally, the reduction in electron density is attributed to the presence of Mo and S vacancies introduced during the growth process. When S vacancies or Mo vacancies are incorporated into the $MoS_2$ lattice, some defect energy levels start to develop in the forbidden gap region, which relates to gradually improved energy bands and electron concentration.[51] As shown by the Raman and XRD analysis, the defect density decreases with an increase in the reaction temperature, indicating a decrease in the electron concentration with an increase in the reaction temperature.

To further confirm the carrier concentration at higher temperature, Mott-Schottky analysis was conducted as using an electrochemical workstation with a three-electrode configuration and a 1 M $Na_2SO_4$ electrolyte solution at room temperature. A silver-silver chloride (Ag/AgCl) electrode served as the reference electrode, while a Pt wire acted as the counter electrode. The $MoS_2$ samples, mixed with a few drops of an ethanol solution, were applied to the surface of a glassy electrode used as the working electrode. By applying a potential bias, an equilibrium at the interface of the electrolyte and working electrode was established, facilitating the transfer of electrons from the semiconductor electrode to the electrolyte.

Figures 3a–3b illustrates the Mott-Schottky curves for the samples, showing positively sloping characteristics that indicate n-type conductivity of the as-prepared $MoS_2$ nanostructures.[52] The flat band potentials were determined by extrapolating the linear portion of the Mott-Schottky curve to the *X*-axis at point $1/C^2 = 0$. The obtained values of the flat band potential were summarized in Table II for $MoS_2-180$ and $MoS_2-220$.

**Table II. Comparison of flat band potential and carrier concentration of as-prepared samples at different temperature 180 and 220 °C.**

| Sample | Flat band potential (V) | Carrier concentration ($cm^{-3}$) |
|---|---|---|
| $MoS_2-180$ | −0.47 | $9.1 \times 10^{19}$ |
| $MoS_2-220$ | −0.45 | $7.3 \times 10^{19}$ |

The carrier concentration of the synthesized samples was also determined from the slope of the linearly fitted Mott-Schottky curve in the potential region −0.4 to 0.2 V, as shown in Figs. 3a–3b. The carrier concentration ($N_D$) was calculated using the equation:

$$N_D = \frac{2}{\epsilon\varepsilon_o}\left[\frac{dV}{d(1/C^2)}\right]$$

where $N_D$ is the carrier concentration, $\varepsilon$ is the dielectric constant of the material, $\varepsilon_o$ is the permittivity of free space, $e$ is the electronic charge, and $dV/d(1/C^2)$ is the slope of the Mott-Schottky curve of the as-synthesized samples. The calculated values of carrier concentrations for $MoS_2-180$ and $MoS_2-220$ samples were presented in Table II.

The relationship between flat band potentials and carrier concentration in nanostructures is indeed influenced by the presence of defects, particularly sulphur vacancies in $MoS_2$. As evidenced by the data in Table II, the $MoS_2-220$ sample exhibited lower values of both carrier concentration and flat band potential compared to the $MoS_2-180$ sample. This significant difference can be attributed to the presence of lower defects, specifically fewer sulphur vacancies, in the $MoS_2-220$ sample. In contrast, samples synthesized at lower temperature demonstrated relatively higher carrier concentrations, primarily due to the influence of sulphur vacancies. These vacancies induced during the synthesis process act as traps, capturing electrons in defect-induced energy states, which results in an increase in carrier (electron) concentration.[53–55] This phenomenon contributes to the higher carrier concentration observed in the $MoS_2-180$ sample. By combining the data from Table II with the results of XRD and Raman analysis, we can assert that the lower value of flat band potential in the $MoS_2-220$ sample, synthesized at 220 °C, can be attributed to the lower carrier concentration resulting from enhanced crystalline quality and reduced sulphur vacancies.[49] Overall, the presence of defects, particularly sulphur vacancies, plays a crucial role in influencing the carrier concentration and, consequently, the flat band potentials in



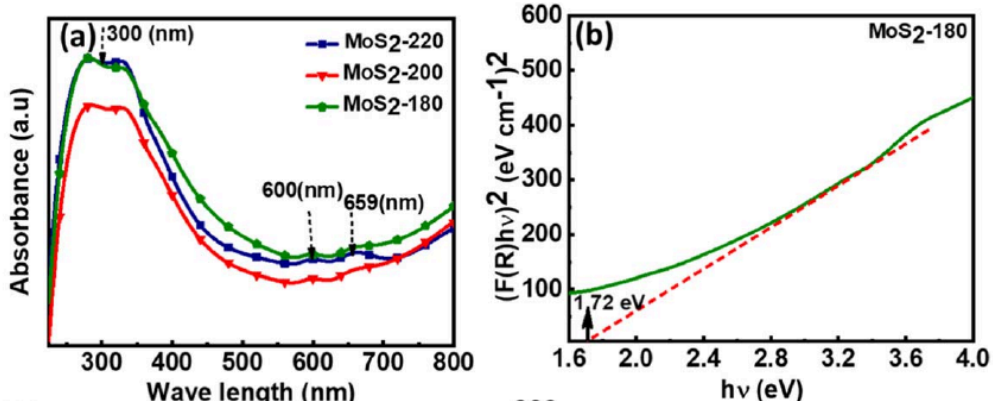

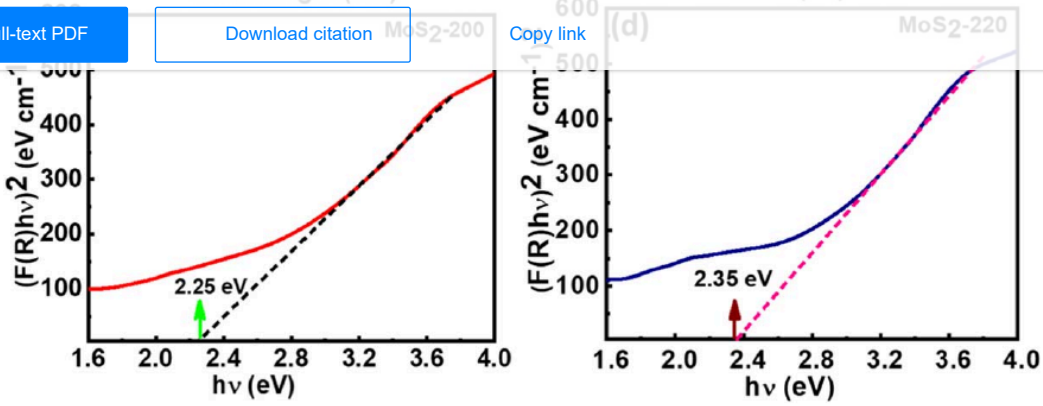


**Figure 4.** (a) Absorbance spectra of $MoS_2$ samples prepared at different temperatures. (b) Diffuse Reflectance Spectroscopy (DRS) plot of $MoS_2$ sample prepared at 180 °C. (c) DRS plot of $MoS_2$ sample prepared at 200 °C. (d) DRS plot of $MoS_2$ sample prepared at 220 °C.

$MoS_2$ nanostructures. The higher crystalline quality and reduced sulphur vacancies in the $MoS_2-220$ sample contribute to the observed lower carrier concentration and flat band potential, highlighting the importance of defect engineering for optimizing the electronic properties of nanomaterials.[56–58]

The optical properties of $MoS_2$ nanostructures synthesized at different temperatures were studied using UV–vis-NIR diffuse reflectance spectroscopy. In the absorbance spectra (Fig. 4a) of the $MoS_2$ samples, a higher absorbance was observed in the UV region compared to the visible region, with the highest peak observed at around 300 nm. This high absorbance is due to inter-band transition of occupied $d_{z^2}$ orbitals to unoccupied $d_{xy-x^2-y^2}$ and $d_{xz-yz}$ orbitals.[59] Two exciton peaks were also observed at 600 and 659 nm, which are attributed to direct band gap transition at K-points of the Brillouin zone.[59,60] It is clearly seen that the appearance of excitonic peaks becomes more intense with an increase in reaction temperature, which is due to the reduction of the number of $MoS_2$ layers with increasing reaction temperature.[31]

The UV- diffuse reflectance spectra of the as-prepared samples were converted into absorption spectra using Kubelka Munk theory:[52,61]

$$F(R_\infty) = \frac{(1-R_\infty)^2}{2R_\infty} = \frac{\alpha}{S}$$

$$R_\infty = \frac{R_{sample}}{R_{standrad}}$$

where F ($R_\infty$), $\alpha$, S, R denote the Kubelka Munk Function, absorption coefficient, scattering coefficient and reflectance, respectively. The optical band gap of $MoS_2$ samples synthesized at different temperatures was determined using the theory of optical transition,

$$F(R_\infty)h\nu = A(h\nu - E_g)^n$$

where hν is the energy of the incident photon, B is the constant for the material, n is the electronic transition (n = 1/2 for direct allowed transition, n = 2 for indirect allowed transition). The Kubelka Munk function was used to determine the value of the absorbance coefficient $\alpha$ from the reflectance spectra of $MoS_2$ samples. However, for the estimation of the band gap of the material, F ($R_\infty$) can be used instead of $\alpha$.[52] The curves of $[F(R_\infty)h\nu]^2$ versus hν were plotted and the optical band gap of $MoS_2$ samples was determined by extrapolation of the linear portion of $[F(R_\infty)h\nu]^2 = 0$.

In Figs. 4b to 4d, we observed a gradual increase in the band gap of $MoS_2$ nanostructures from 1.72 to 2.35 eV as the reaction temperature increased from 180 to 220 °C. This trend in the band gap modulation can be attributed to the decrease in the number of $MoS_2$ layers as the reaction temperature increased, a phenomenon supported by previous studies.[49,62,63]

The Raman analysis further validated this observation, revealing a decrease in the number of layers as indicated by the position difference of Raman active peaks of $MoS_2$ from 180 °C to 220 °C. The increase in the band gap of the nanostructures can be attributed to the well-known quantum confinement effect, a key aspect in low-dimensional materials.[64,65] Quantum confinement restricts the motion of electrons to specific energy levels within the reduced dimensionality of the material. As the $MoS_2$ transitions from a bulk (3D) structure to a 2D structure, the decrease in the confining dimensionality results in the formation of discrete energy levels,



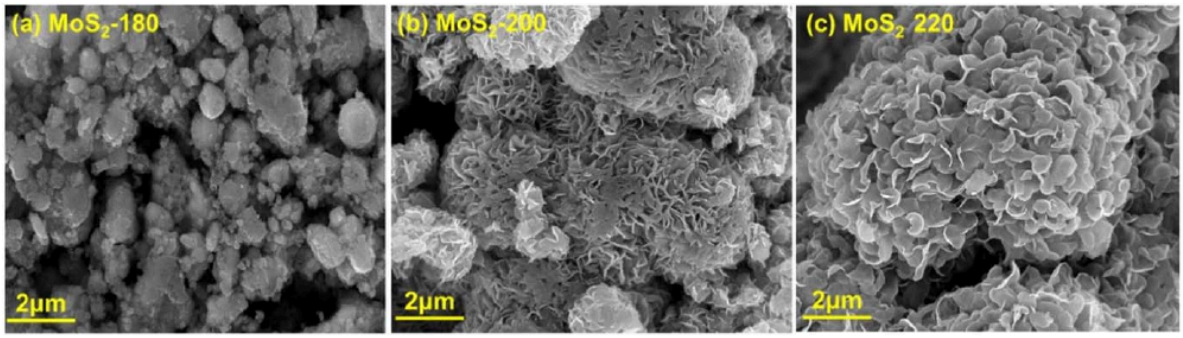


**Figure 5.** FESEM images of $MoS_2$ nanostructures synthesized at different temperatures (a) 180 °C (b) 200 °C and (c) 220 °C.

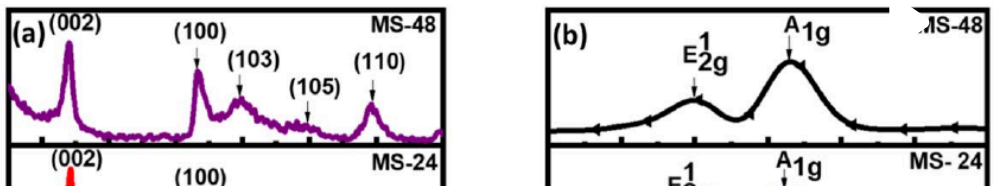

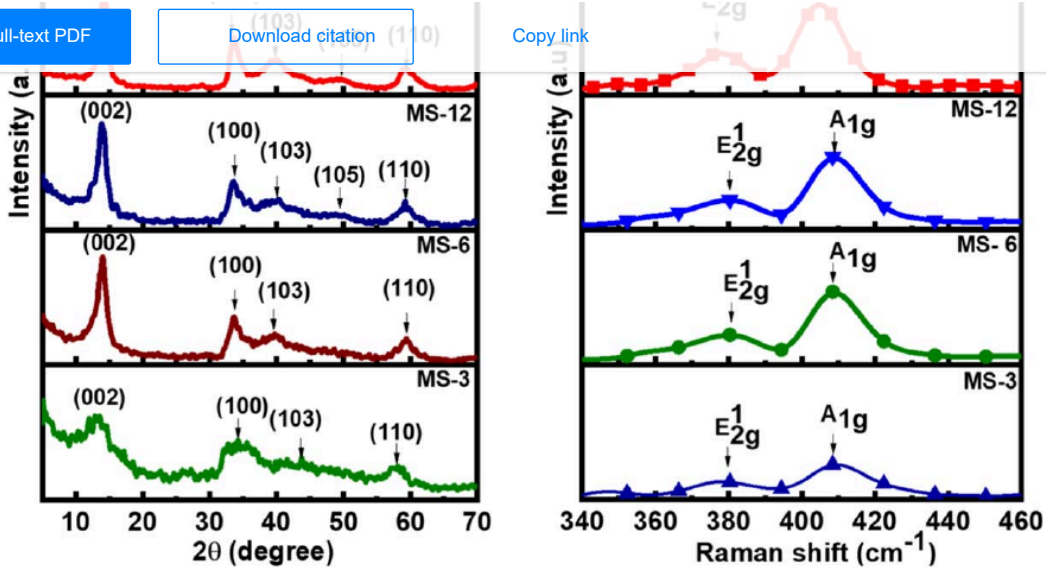


**Figure 6.** (a) XRD and (b) Raman spectra of $MoS_2$ samples synthesized at different reaction time of 3 (MS-3), 6 (MS-6), 12 (MS-12), 24 (MS-24) and 48 (MS-48) h.

leading to a splitting of energy levels due to quantum confinement. This energy level splitting ultimately leads to the widening of the band gap in the material. Our findings on the band gap values of various $MoS_2$ nanostructures are consistent with reported values in the literature, which range from 1.58 to 2.35 eV.[24,49,53] These findings provide valuable insights into the tunability of the band gap of $MoS_2$ nanostructures, holding significant implications for their potential applications in various electronic and optoelectronic devices.[23,42,66]

The morphologies of the as-prepared samples were investigated using a field emission scanning electron microscope (FESEM) and are provided in Fig. 5. The results clearly demonstrate that the surface morphology of the samples can be improved with an increase in reaction temperature. As the reaction temperature increases, the nanoflowers exhibit a more voluminous structure, accompanied by a noticeable reduction in the thickness of the constituent nanosheets, a trend that is also corroborated by the Raman analysis. It is worth mentioning that the fluffy nature of the nanoflowers can provide more void space, which could be beneficial in many of applications, such as gas sensing and biosensing, energy storage and conversion, photocatalytic activities, etc.[43,48]

***Influence of reaction time.***—To investigate the impact of reaction time on the properties of $MoS_2$ nanostructures, various reaction durations of 3, 6, 12, 24, and 48 h were employed at a consistent reaction temperature of 220 °C, which had been optimized in the preceding section. Figure 6a showcases the X-ray diffraction pattern of $MoS_2$ samples synthesized under different reaction times: 3 (MS-3), 6 (MS-6), 12 (MS-12), 24 (MS-24), and 48 (MS-48) h. The diffraction peaks of all samples demonstrate the pure $MoS_2$



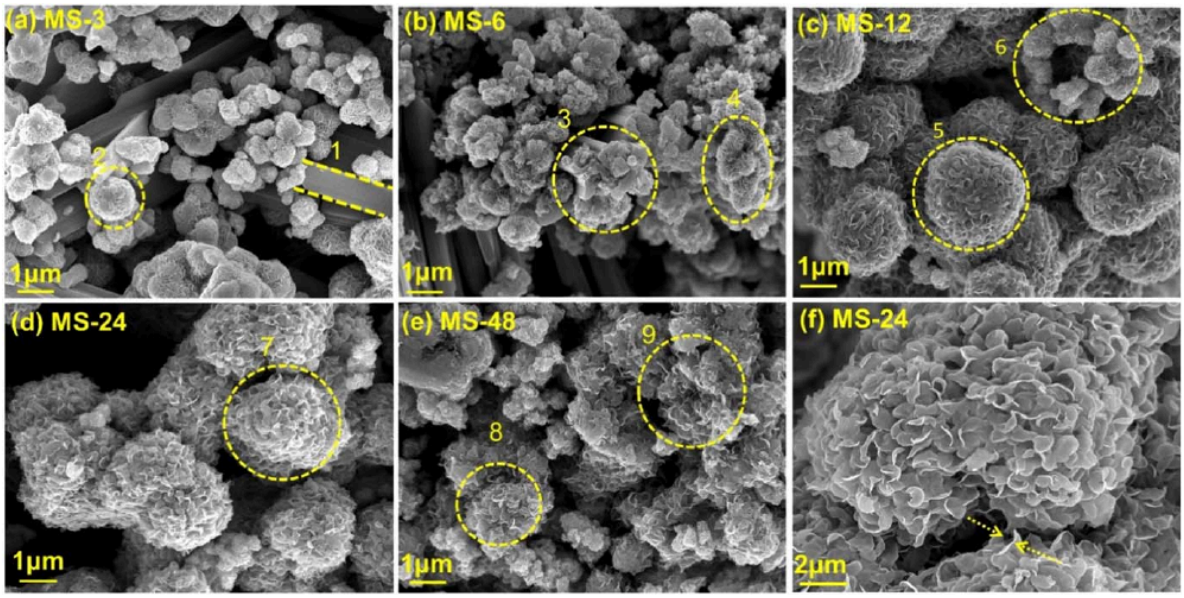


**Figure 7.** FESEM micrographs of $MoS_2$ nanostructures prepared with 3 h (a) 6 h (b) 12 h (c) 24 h (d) 48 h (e), (f) 24 h at higher magnification.

**Table III. Comparison of diffraction angle (2$\theta$), interlayer spacing (d), crystallite sizes (D), lattice parameters (a, c), microstrain ($\varepsilon$) and dislocation density ($\delta$) of as synthesized samples with different time duration.**

| Sample | 2$\theta$ (hkl) | d (nm) | D (nm) | a (Å) | c (Å) | $\varepsilon$ | $\delta(1\times10^{15}/m^{-2}$ |
|---|---|---|---|---|---|---|---|
| M-3 | 13.47° (002) | 0.657 | 4.64 | 3.06 | 13.13 | 0.033 | 46.4 |

| | | | | | | | |
|---|---|---|---|---|---|---|---|
| M-48 | 14.05° (002) | 0.629 | 8.17 | 3.08 | 12.54 | 0.006 | 14.9 |

phase and align with JCPDS data (37–1492).[28,44] The sample synthesized for 3 h (MS-3) displays a low-intensity, broad diffraction peak at 13.47°, corresponding to the (002) plane of the 2H phase of the $MoS_2$ crystal. The subdued intensity and broadness of this peak can be attributed to a smaller crystallite size. As the reaction time increases, the intensity of this peak augments, indicating an improvement in crystalline quality and the formation of well-stacked layers of $MoS_2$ nanostructures along the *c*-axis.[33]

Furthermore, the shift in the peak position of the (002) plane towards a higher angle of $2\theta$ with prolonged reaction time results in a reduced interplanar spacing of samples synthesized for an extended duration, affirming the heightened purity of the synthesized samples.

Table III presents the escalating crystallite size and diminishing interplanar spacing for $MoS_2$ samples prepared with longer reaction times. The table also provides microstrain and dislocation density calculations derived from XRD data. It is evident from Table III that $MoS_2$ nanostructures synthesized for 24 h at 220 °C exhibit superior crystallite quality and lower defect density. This favourable outcome can be attributed to the presence of smaller microstrain (0.004) and dislocation density (13.7 $m^{-2}$) at a reaction temperature of 220 °C for a duration of 24 h.[49]

Furthermore, Raman analysis was employed to investigate the influence of various reaction times on the structural properties of $MoS_2$ samples. As depicted in Fig. 6b, all the samples prepared with different reaction times exhibited two characteristic peaks of $MoS_2$ at 378 and 404 $cm^{-1}$.[21] As previously discussed, the difference in the $E^1_{2g}$ and $A_{1g}$ peak positions were utilized to evaluate the number of $MoS_2$ layers. The difference in the peaks position with reaction time of 3, 6, 12, 24 and 48 h were found to be 31, 29, 27, 26 and 27 $cm^{-1}$, respectively. It can be observed that the peaks difference first decreases with an increase in the reaction time from 3 to 24 h, and then it increases as the reaction time increases from 24 to 48 h. This reduction in peaks difference indicates a reduction in $MoS_2$ layers, as discussed earlier. It is worth noting that the sample prepared with 24 h has a smaller number of layers with better crystalline quality due to a smaller FWHM of $E^1_{2g}$ which was also confirmed by XRD data.

FESEM images of $MoS_2$ nanostructures synthesized at different reaction times are presented in Figs. 7a–7f. The images clearly demonstrate that the surface morphology of $MoS_2$ samples can be significantly modified by varying the reaction time. $MoS_2$ nanostructures synthesized for shorter reaction times of 3 and 6 h mostly consist of nanorod-like structures, as shown in Fig. 7a, denoted by numeric symbol 1 (dotted line). Some flower-like structures also start to form at the end of the nanorods, as depicted in Fig. 7b and indicated by numeric symbol 3 (dotted circle). These rod-like nanostructures are believed to have occurred due to incomplete dissolution of Mo precursor during the shorter reaction time. As the reaction time is increased from 6 to 12 h, the rod-like nanostructures disappear completely, and some flower-like structures with small petals appear (marked by numeric symbol 6), as shown in Fig. 7c and denoted by numeric symbol 5. Interestingly, flowers with bigger and thinner petals are formed when the synthesis time increases from 12 h to 24 h. The nanosheets become thinner for samples grown for



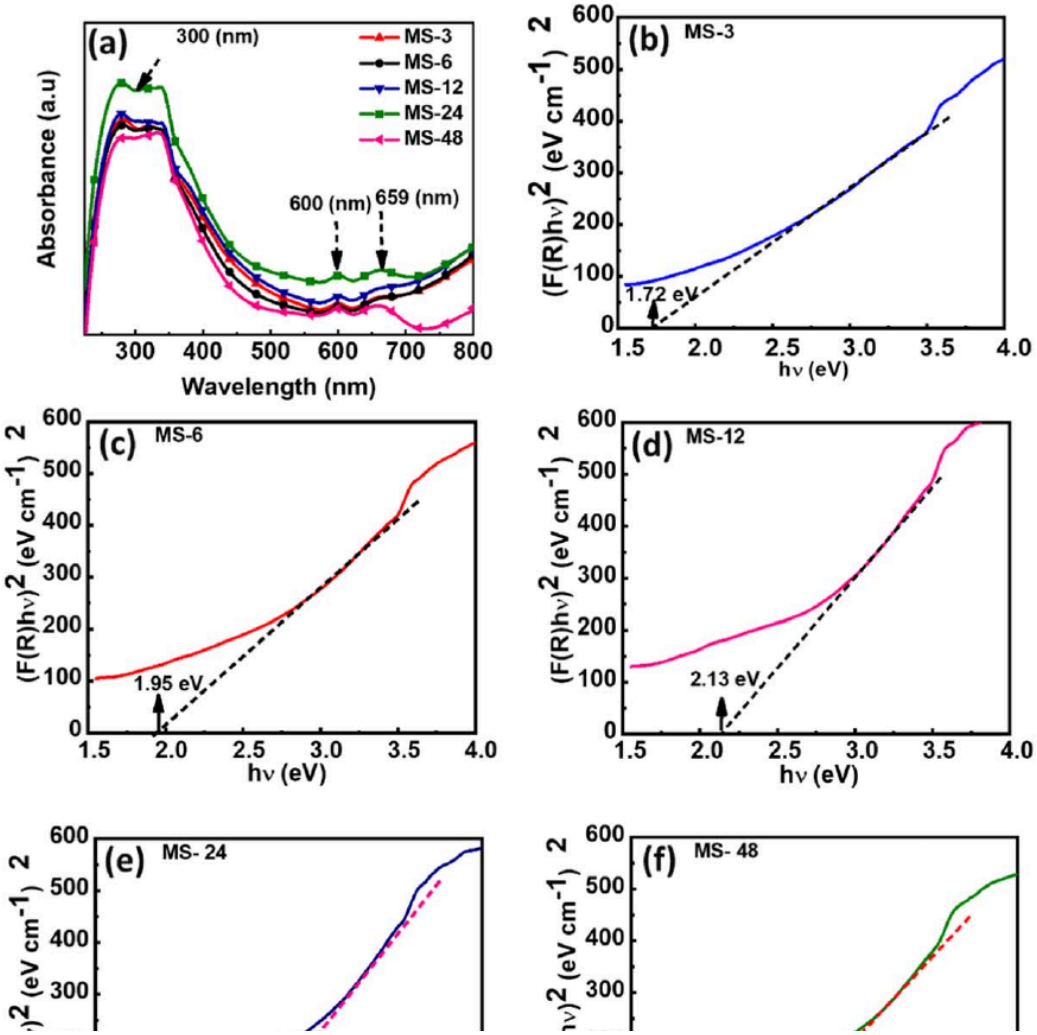

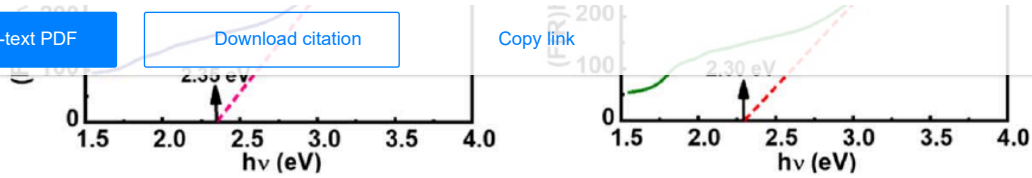


**Figure 8.** (a) Absorbance and (b-f) diffuse reflectance spectra of $MoS_2$ samples synthesized with different reaction time.

24 h, as indicated by yellow arrows in Fig. 7f at higher magnification. The increase in nanoflower size is due to the fact that as the reaction time increases, self-assembly of nanosheets also increases. A plausible growth mechanism for the formation of 3D flower-like structures is explained in the Growth Mechanism section of this study. However, the sample prepared for 48 h consists of nanoflowers with non- uniform $MoS_2$ nanosheets. Hence, when the reaction temperature is prolonged to 48 h, the 3D flowers gradually diminished and disperse into interconnected nanosheets denoted by the yellow circle with numeric symbols 8 and 9 in Fig. 7e.

The UV–vis-NIR absorbance spectra and diffuse reflectance spectroscopy (DRS) plots for band gap calculation of the as-prepared $MoS_2$ samples are depicted in Fig. 8.

As shown in Fig. 8a, the intensities of excitonic peaks at 600 and 659 nm increase with an increase in reaction time.[67] This is attributed to a reduction in the number of $MoS_2$ layers with an increase in the reaction time, as discussed earlier. Interestingly, the value of the band gap of $MoS_2$ nanostructures first increases from 1.72 to 2.35 eV as the reaction time increases from 3 to 24 h, but then the value of the band gap decreases as we increase the reaction time from 24 to 48 h. This decrease in the band gap with an increase in the reaction time from 24 to 48 h was attributed to an increase in the number of layers, which was also confirmed by Raman analysis. As discussed previously, the decrease in the number of layers with an increase in the band gap can be attributed to the quantum confinement effect in 2D $MoS_2$ nanosheets.

***Growth mechanism.***—Based on various structural and morphological findings, the most possible growth mechanism for 3D flower-like $MoS_2$ nanostructures formed by the stacking of thin



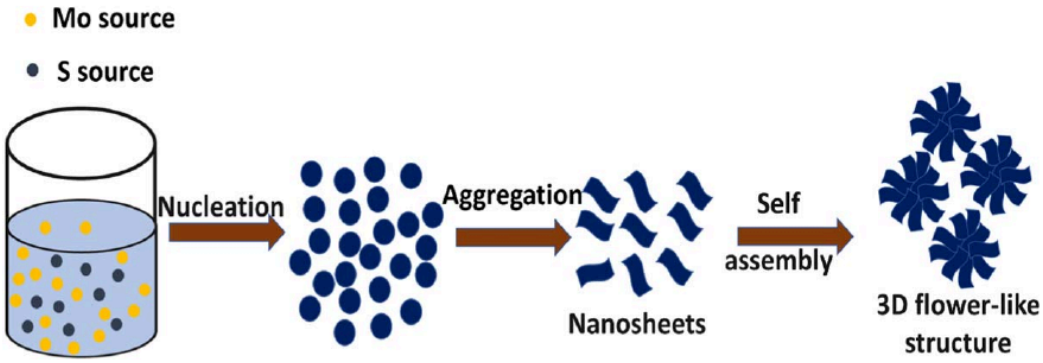


**Figure 9.** Growth mechanism of 3D flower- like $MoS_2$ nanostructures.

$MoS_2$ nanosheets has been proposed as shown schematically in Fig. 9. The growth process can be divided into three steps: (i) nucleation, (ii) aggregation in nanosheets, and (iii) self-assembly of nanosheets resulting in the formation of nanoflowers. Initially in the presence of water, Mo $[(NH_4)_6Mo_7O_{24}.4H_2O]$ and S $[CH_4N_2S]$ sources collide elastically and form a transparent homogeneous solution at room temperature. In the next step, the hydrothermal process generates $H_2S$ gas by hydrolysis of thiourea, which creates high pressure leading to the formation of $MoS_2$ nuclei. These $MoS_2$ nuclei grow over time and form S-Mo-S layers. It is worth noting that hydrothermal temperature should be between the boiling point and critical temperature of water. Thereafter, the aggregation of primary $MoS_2$ nuclei due to high stress leads to the formation of nanosheets. These nanosheets form the basis for the formation of nanoflowers via the self-assembly process. Furthermore, as the hydrothermal temperature is increased, the nuclei begin to form bigger in size resulting in better quality of crystal of $MoS_2$ nanoflowers, as indicated by the structural and morphological analysis. This is because the critical nuclei size increases with an increase in temperature and the barrier for nucleation is greater with increasing temperature. Therefore, an increase in temperature hinders the initiations of nucleation for new nuclei, and as a result, the earlier formed nuclei begin to increase in size.[68] However, when synthesis time is increased beyond a typical value (here it is 24 h), the morphology of 3D flower-like nanostructures becomes uneven due to the effect of high stress for longer duration, as evident by the Fig. 7e.

## Conclusions

The 3D flower-like $MoS_2$ nanostructures were successfully synthesized via a facile hydrothermal method at diverse temperatures and times. This 3D flower-like morphology of $MoS_2$ nanostructure was found to be formed due to a nucleation-oriented self-assembly growth process. The influence of reaction temperature and

## Author Contributions

R. Kumari carried out the experimental research work towards synthesis and characterization of $MoS_2$ nanostructures. The present study was conceived and supervised by R. Kumar, Assistant Professor, Department of Physics and Astrophysics, Central University of Haryana, Mahendragarh, India.

## Funding

This research was supported by the Start-Up research grant provided by UGC, Government of India.

## Data Availability

The authors declare that the data supporting the findings of this study are available within the article. Complementary data relevant for the present study are available from the corresponding author upon reasonable request.

## Competing Interest

The authors have no relevant financial or non-financial interests to disclose.

## ORCID

Rakesh Kumar https://orcid.org/0000-0003-2367-4545

## References

1. D. Sarkar et al., "Functionalization of transition meta chalcogenides with metallic nanoparticles: implications for doping and gas-sensing." *Nano Lett.*, **15**, 2852 (2015).
2. W. Li et al., "Flowerlike WSe2 and WS2 microspheres: one-pot synthesis, formation mechanism and application in heavy metal ion sequestration." *Chem. Commun.*, **52**, 4481 (2016).
3. Z. Lin et al., "Solution-processable 2D semiconductors for high-performance large-area electronics." *Nature*, **562**, 254 (2018).

interplanar spacing, fewer defects, and a uniform flower-like morphology. The results of this study strongly suggest that the reaction temperature and duration for the synthesis of $MoS_2$ nanostructures play an important role. These findings propose the future use of $MoS_2$ nanostructures in different applications, including gas and biosensing, energy storage and conversion, as well as photocatalyst for hydrogen evolution reaction and degradation of organic pollutants.

## Acknowledgments

The support provided by UGC, Government of India, is acknowledged. One of the authors, Ritu Kumari, is thankful to Central University of Haryana for providing research fellowship.


4. A. Gautam, "Towards modern-age advanced sensors for the management of neurodegenerative disorders: current status, challenges and prospects." *ECS Sensors Plus*, 1, 042401 (2022).
5. A. Turner, "Perspective-an age of sensors." *ECS Sensors Plus*, **1**, 011601 (2022).
6. V. Chaudhary, A. Kaushik, H. Furukawa, and A. Khosla, "Towards 5th generation AI and IOT driven sustainable intelligent sensors based on 2d mxenes and borophene." *ECS Sensors Plus*, **1**, 013601 (2022).
7. G. Barik and S. Pal, "Defect induced performance enhancement of monolayer MoS2 for Li-and Na-ion batteries." *The Journal of Physical Chemistry C*, **123**, 21852 (2019).
8. X. Cao, C. Tan, X. Zhang, W. Zhao, and H. Zhang, "Solution-processed two-dimensional metal dichalcogenide-based nanomaterials for energy storage and conversion." *Adv. Mater.*, **28**, 6167 (2016).
9. R. Kumar, N. Goel, M. Hojamberdiev, and M. Kumar, "Transition metal dichalcogenides-based flexible gas sensors." *Sens. Actuators, A*, **303**, 111875 (2020).
10. L. Yin, X. Hai, K. Chang, F. Ichihara, and J. Ye, "Synergetic exfoliation and lateral size engineering of MoS2 for enhanced photocatalytic hydrogen generation." *Small*, **14**, 1704153 (2018).
11. T. Q. Casuse et al., "DC sputtered ultralow loading gold nanofilm electrodes for detection of As (III) in water." *ECS Sensors Plus*, **1**, 014602 (2022).





12. S. Agrohiya et al., "Nickel doped zinc oxide thin films for visible blind ultraviolet photodetection applications." *ECS Sensors Plus*, **1**, 043601 (2022).
13. A. Singh, A. Verma, and B. Yadav, "MnO2-SnO2 based liquefied petroleum gas sensing device for lowest explosion limit gas concentration." *ECS Sensors Plus*, **1**, 025201 (2022).
14. N. Tyagi, M. K. Singh, and M. Khanuja, "Synergistic effect of polypyrrole modified WS2 nanosheets on visible light assisted catalysis for the removal of chromium (VI) and humic acid." *Mater. Res. Bull.*, **163**, 112216 (2023).
15. M. Liang et al., "Improving stability of organometallic-halide perovskite solar cells using exfoliation two-dimensional molybdenum chalcogenides." *npj 2D Materials and Applications*, **4**, 1 (2020).
16. Y. Zhang, W. Zeng, and Y. Li, "The hydrothermal synthesis of 3D hierarchical porous MoS2 microspheres assembled by nanosheets with excellent gas sensing properties." *J. Alloys Compd.*, **749**, 355 (2018).
17. W.-B. Xu, B.-J. Huang, P. Li, F. Li, C.-W. Zhang, and P.-J. Wang, "The electronic structure and optical properties of Mn and B, C, N co-doped MoS2 monolayers." *Nanoscale Res. Lett.*, **9**, 1 (2014).
18. K-A. N. Duerloo, Y. Li, and E. J. Reed, "Structural phase transitions in two-dimensional Mo-and W-dichalcogenide monolayers." *Nat. Commun.*, **5**, 1 (2014).
19. M. Placidi et al., "Multiwavelength excitation Raman scattering analysis of bulk and two-dimensional MoS2: vibrational properties of atomically thin MoS2 layers." *2D Mater.*, **2**, 035006 (2015).
20. H. Zuoli and Q. Wenxiu, "Molybdenum disulfide nanomaterials: Structures, properties, synthesis and recent progress on hydrogen evolution reaction." *Applied Materials Today*, **3**, 23 (2016).
21. Y. Lu, X. Yao, J. Yin, G. Peng, P. Cui, and X. Xu, "MoS2 nanoflowers consisting of nanosheets with a controllable interlayer distance as high-performance lithium ion battery anodes." *RSC Adv.*, **5**, 7938 (2015).
22. H. Cao, Z. Bai, Y. Li, Z. Xiao, X. Zhang, and G. Li, "Solvothermal synthesis of defect-rich mixed 1T-2H MoS2 nanoflowers for enhanced hydrodesulfurization." *ACS Sustainable Chemistry & Engineering*, **8**, 7343 (2020).
23. Y. L. Huang et al., "Bandgap tunability at single-layer molybdenum disulphide grain boundaries." *Nat. Commun.*, **6**, 6298 (2015).
24. N. Kumar et al., "Probing into crystallography and morphology properties of MoS2 nanoflowers synthesized via temperature dependent hydrothermal method." *Nano Express*, **3**, 035001 (2022).
25. R. Fan et al., "A strategy for accessing nanobody-based electrochemical sensors for analyte detection in complex media." *ECS Sensors Plus*, **1**, 010601 (2022).
26. T. Hyodo, W. Sakata, T. Ueda, and Y. Shimizu, "Effects of surface modification of platinum electrodes with gold on hydrogen-sensing properties of diode-type sensors." *ECS Sensors Plus*, **1**, 013602 (2022).
27. S. K. Das, K. K. Nayak, P. Krishnaswamy, V. Kumar, and N. Bhat, "Electrochemistry and other emerging technologies for continuous glucose monitoring devices." *ECS Sensors Plus* (2022).
28. N. Kumar et al., "Probing on crystallographic structural and surface morphology of hydrothermally synthesized MoS2 nanoflowers consisting of nanosheets." *Applied Surface Science Advances*, **6**, 100167 (2021).
29. X. Yang, L. Wen, H. Huang, Y. Wang, L. Wei, and J. Yang, "Hydrothermal synthesis of MoS2 nanoflowers and its rapid adsorption of tetracycline." *Solid State Sci.*, **133**, 107014 (2022).
30. N. Chaudhary, M. Khanuja, and S. Islam, "Hydrothermal synthesis of MoS2 nanosheets for multiple wavelength optical sensing applications." *Sens. Actuators, A*, **277**, 190 (2018).
31. X. Qiu, T. Zhang, Z. Dai, R. Cao, and T. Wei, "Effect of one-step hydrothermal reaction conditions on the crystal growth of nano-/micro-MoS2." *Ionics*, **28**, 939 (2022).
32. P. Chen, J. Hu, M. Yin, W. Bai, X. Chen, and Y. Zhang, "MoS2 nanoflowers decorated with au nanoparticles for visible-light-enhanced gas sensing." *ACS Appl. Nano Mater.* (2021).
33. M. Vidhya, T. Selvakumari, R. Marnadu, I. Ashraf, and M. Shkir, "Impact of temperature on the properties of MoS2 nanoflakes synthesized by facile hydrothermal method for electrochemical supercapacitor applications." *Inorg. Chem. Commun.*, **145**, 109928 (2022).
34. J. Jaiswal, P. Tiwari, P. Singh, and R. Chandra, "Fabrication of highly responsive room temperature H2 sensor based on vertically aligned edge-oriented MoS2 nanostructured thin film functionalized by Pd nanoparticles." *Sensors Actuators B*, **325**, 128800 (2020).
35. T. Oztas, H. S. Sen, E. Durgun, and B. L. Ortaç, "Synthesis of colloidal 2D/3D MoS2 nanostructures by pulsed laser ablation in an organic liquid environment." *The Journal of Physical Chemistry C*, **118**, 30120 (2014).
36. K. Sheybani and S. Javadpour, "Mechano-thermal reduction of molybdenite ($MoS2$) in the presence of Sulfur scavenger: new method for production of molybdenum carbide." *Int. J. Refract. Met. Hard Mater*, **92**, 105277 (2020).
37. R. Kumar et al., "Plasmonic Au nanoparticles sensitized $MoS_2$ for bifunctional $NO_2$ and light sensing." *IEEE Sens. J.*, **21**, 4190 (2021).
39. L. Ma et al., "SDBS-assisted hydrothermal preparation and electrocatalytic properties of few-layer and edge-rich MoS2 nanospheres." *Superlattices Microstruct.*, **83**, 112 (2015).
40. X. Zhang et al., "Hydrothermal synthesis and characterization of 3D flower-like MoS2 microspheres." *Mater. Lett.*, **148**, 67 (2015).
41. N. Kiomarsipour and R. S. Razavi, "Characterization and optical property of ZnO nano-, submicro-and microrods synthesized by hydrothermal method on a large-scale." *Superlattices Microstruct.*, **52**, 704 (2012).
42. X. Zhang et al., "Photocatalytic activity of 3D flower-like MoS2 hemispheres." *Mater. Res. Bull.*, **100**, 249 (2018).
43. N. T. Thang, N. H. Thoan, C. M. Hung, N. Van Duy, N. Van Hieu, and N. D. Hoa, "Controlled synthesis of ultrathin $MoS_2$ nanoflowers for highly enhanced $NO_2$ sensing at room temperature." *RSC Adv.*, **10**, 12759 (2020).
44. G. Li et al., "Synthesis and characterization of hollow MoS2 microspheres grown from MoO3 precursors." *J. Alloys Compd.*, **501**, 275 (2010).
45. Z. Yu et al., "Towards intrinsic charge transport in monolayer molybdenum disulfide by defect and interface engineering." *Nat. Commun.*, **5**, 1 (2014).
46. H. Li, F. Xie, W. Li, B. D. Fahlman, M. Chen, and W. Li, "Preparation and adsorption capacity of porous MoS2 nanosheets." *RSC Adv.*, **6**, 105222 (2016).
47. J. Xie et al., "Controllable disorder engineering in oxygen-incorporated MoS2 ultrathin nanosheets for efficient hydrogen evolution." *J. Am. Chem. Soc.*, **135**, 17881 (2013).
48. S. Liang et al., "PVP-assisted synthesis of MoS 2 nanosheets with improved lithium storage properties." *CrystEngComm*, **15**, 4998 (2013).
49. E. Ghaleghafi, M. B. Rahmani, and Z.-H. Wei, "Photoluminescence and UV photosensitivity of few-layered $MoS_2$ nanosheets synthesized under different hydrothermal growth times." *J. Mater. Sci.*, **56**, 11749 (2021).
50. C. Yang, B. Wang, Y. Xie, Y. Zheng, and C. Jin, "Deriving MoS2 nanoribbons from their flakes by chemical vapor deposition." *Nanotechnology*, **30**, 255602 (2019).
51. Y. Xie et al., "Defect engineering of MoS2 for room-temperature terahertz photodetection." *ACS Appl. Mater. Interfaces*, **12**, 7351 (2020).
52. A. Lamouchi, I. B. Assaker, and R. Chtourou, "Effect of annealing temperature on the structural, optical, and electrical properties of MoS2 electrodeposited onto stainless steel mesh." *J. Mater. Sci.*, **52**, 4635 (2017).
53. S. Bolar, S. Shit, N. C. Murmu, P. Samanta, and T. Kuila, "Activation strategy of MoS2 as HER electrocatalyst through doping-induced lattice strain, band gap engineering, and active crystal plane design." *ACS Appl. Mater. Interfaces*, **13**, 765 (2021).
54. S. Bolar et al., "Optimization of active surface area of flower like MoS2 using V-doping towards enhanced hydrogen evolution reaction in acidic and basic medium." *Appl. Catalysis B*, **254**, 432 (2019).
55. W. T. Yein, Q. Wang, Y. Liu, Y. Li, J. Jian, and X. Wu, "Piezo-potential induced molecular oxygen activation of defect-rich MoS2 ultrathin nanosheets for organic dye degradation in dark." *J. Environ. Chem. Eng.*, **8**, 103626 (2020).
56. K. Cho et al., "Electrical and optical characterization of MoS2 with sulfur vacancy passivation by treatment with alkanethiol molecules." *ACS nano*, **9**, 8044 (2015).
57. R. Addou, L. Colombo, and R. M. Wallace, "Surface defects on natural MoS2." *ACS Appl. Mater. Interfaces*, **7**, 11921 (2015).
58. J. Hong, C. Jin, J. Yuan, and Z. Zhang, "Atomic defects in two-dimensional materials: From single-atom spectroscopy to functionalities in opto-/electronics, nanomagnetism, and catalysis." *Adv. Mater.*, **29**, 1606434 (2017).
59. F. O. V. Gomes et al., "Influence of temperature on morphological and optical properties of MoS2 layers as grown based on solution processed precursor." *Thin Solid Films*, **645**, 38 (2018).
60. A. Michail et al., "Controllable, eco-friendly, synthesis of highly crystalline 2D-MoS2 and clarification of the role of growth-induced strain." *2D Mater.*, **5**, 035035 (2018).
61. Y. C. Zhang, J. Li, M. Zhang, and D. D. Dionysiou, "Size-tunable hydrothermal synthesis of SnS2 nanocrystals with high performance in visible light-driven photocatalytic reduction of aqueous Cr (VI)." *Environmental science & technology*, **45**, 9324 (2011).
62. E. Singh, K. S. Kim, G. Y. Yeom, and H. S. Nalwa, "Atomically thin-layered molybdenum disulfide (MoS2) for bulk-heterojunction solar cells." *ACS Appl. Mater. Interfaces*, **9**, 3223 (2017).
63. Z. Wang, *MoS2: Materials, Physics, and Devices* (Springer, New York Dordrecht London) (2014).
64. Z. Gan et al., "Quantum confinement effects across two-dimensional planes in MoS2 quantum dots." *Appl. Phys. Lett.*, **106**, 23 (2
65. X. Zhu et al., "Probing quantum confinement effect on the excitonic property and electronic band structures of MoS2." *Appl. Surf. Sci.*, **519**, 146262 (2020).
66. G. Dushaq, B. Paredes, J.-Y. Lu, M. Chiesa, and M. Rasras, "Tuning the Photoluminescence of Few-Layer MoS2 Nanosheets by Mechanical Nanostamping for Broadband Optoelectronic Applications." *ACS Appl. Nano Mater.*, **3**, 10333 (2020).
67. A. Arora, K. Sharma, and S. Tripathi, "Influence of reaction temperature, time and molar ratio on hydrothermal synthesis of MoS 2 nanosheets." *Digest Journal of*

MoS2. ACS A... 7, 2952 (2015). ... L. Chopra, Thin Film Phenomena (McGraw-Hill, New York) (1969).

Recommended publications Discover more

Article Full-text available

Enhanced photocatalytic degradation of Cr (VI) and organic pollutants using novel 3D/2D MoS2/SnS2 he...

September 2024 · Physica Scripta

Ritu Kumari · Rakesh Kumar

In this study, 3D flower-like MoS2 nanostructures were synthesized using a hydrothermal technique to form heterostructures with 2D porous SnS2 nanosheets. The resulting 3D/2D MoS2/SnS2 heterostructures were evaluated for their photocatalytic abilities in removing Cr (VI), tetracycline (TC), and methylene blue (MB) under simulated solar irradiation. The results demonstrate that the MoS2/SnS2 ... [Show full abstract]

View full-text

Article Full-text available

Review—Recent Advances in MoS2 and Its Derivatives-Based Two-Dimensional Gas Sensors

September 2022 · ECS Journal of Solid State Science and Technology

Ritu Kumari · Rakesh Kumar

Sensing of hazardous gases is one of the most significant challenge in front of humans in this technological era, because degradation of eminence air, due to emission of diverse air contaminants by urbanization activities, is increasing day by day. There is an urgent global demand of advanced materials with enhanced sensing features for monitoring the pollutants to prevent the environmental ... [Show full abstract]

View full-text

Article Full-text available

Probing into crystallography and morphology properties of MoS2 nanoflowers synthesized via temperatu...

July 2022 · Nano Express

Naveen Kumar · Piyush Siroha · Hari Shankar · [...] · Jitendra Gangwar

This paper reports the formation of flower-like hierarchical molybdenum disulfide (MoS2) nanoparticles following a simple one-step hydrothermal process with varying temperatures (200 ºC and 220 ºC). The as-synthesized particles were examined crystallographically by x-ray diffraction (XRD) method which revealed the formation of hexagonal MoS2 (2H-MoS2). and that the crystallite size of the ... [Show full abstract]

View full-text

Article

Impact of Thermal Ramp Rate on Structural and Photocatalytic Properties of 3D Flower-like MoS2 Nanos...

September 2024 · Hybrid Advances

Ritu Kumari · Rakesh Kumar

Read more

Last Updated: 29 Jul 2024